Multi-exponential MRI T2 maps: A tool to classify and characterize fruit tissues

Guylaine Collewet, Maja Musse, Christian El Hajj, Saïd Moussaoui

Abstract

The estimation of multi-exponential relaxation time T_2 and their associated amplitudes A_0 at the voxel level has been made possible by recent developments in the field of image processing. These data are of great interest for the characterization of biological tissues, such as fruit tissues. However, they represent a high number of information, not easily interpretable. Moreover, the non-uniformity of the MRI images, which mainly directly impacts A_0, could induce interpretation errors. In this paper, we propose a post-processing scheme that clusters similar voxels according to the multi-exponential relaxation parameters in order to reduce the complexity of the information while avoiding the problems associated with intensity non-uniformity. We also suggest a data representation suitable for the visualization of the multi-T_2 distribution within each tissue. We illustrate this work with results for different fruits, demonstrating the great potential of multi-T_2 information to shed new light on fruit characterization.

Multi-exponential MRI T2 maps: a tool to classify and characterize fruit tissues

Authors : Guylaine Collewet*[1], Maja Musse[1], Christian El Hajj[1,2], Saïd Moussaoui[2]

*Corresponding author : guylaine.collewet@inrae.fr

1 INRAE, OPAALE, F-35044 Rennes, France, and

2 Ecole Centrale Nantes, LS2N UMR CNRS 6004, F-44321 Nantes,

Figure 1

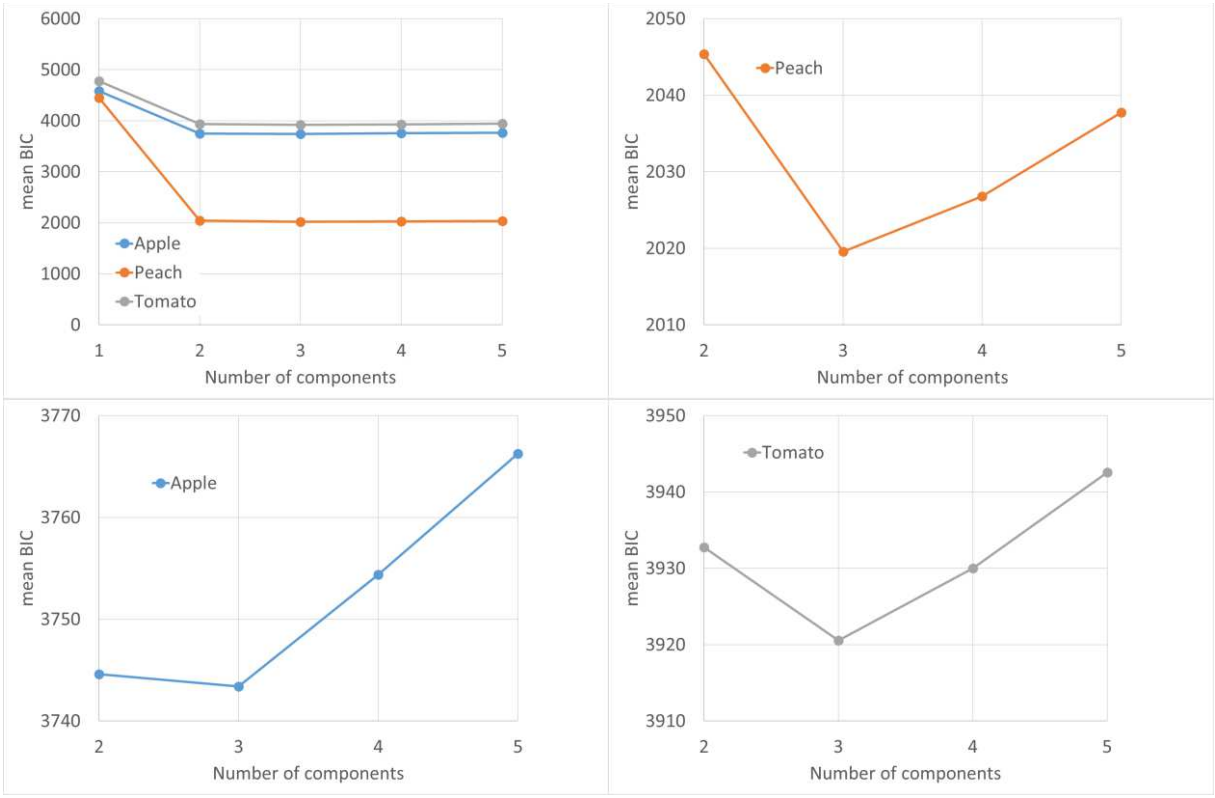

Figure 2

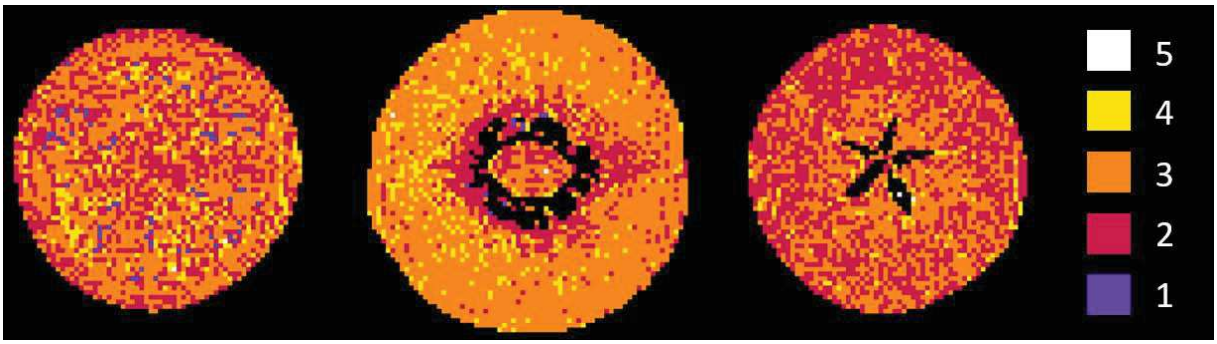

Figure 3

Click here to access/download;Figure;figure_3.docx

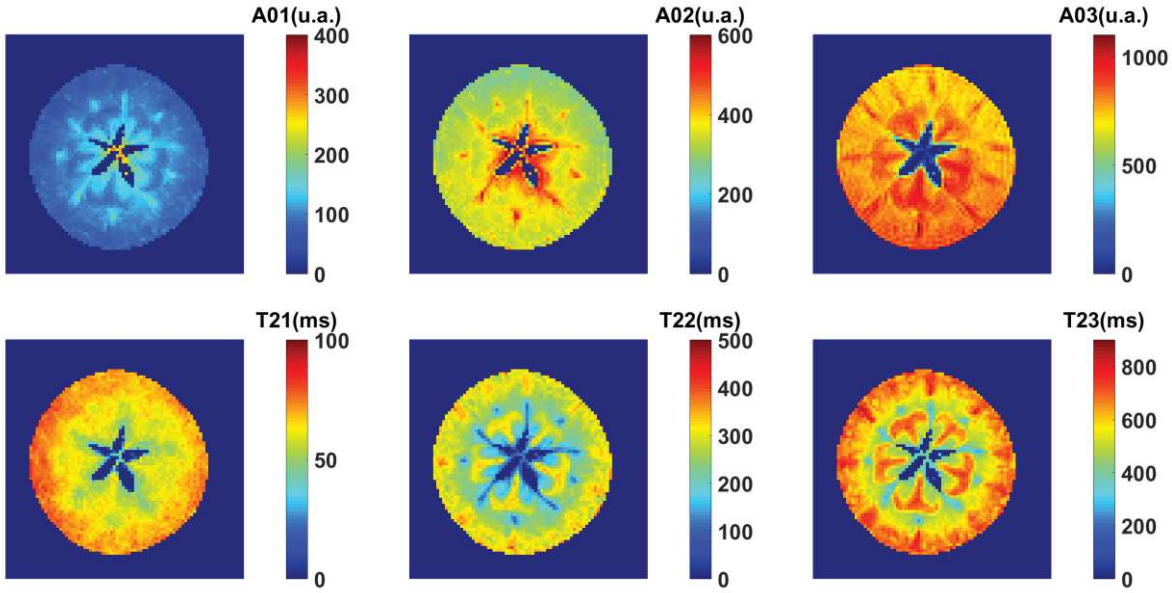

Figure 4

Click here to access/download;Figure;figure_4.docx

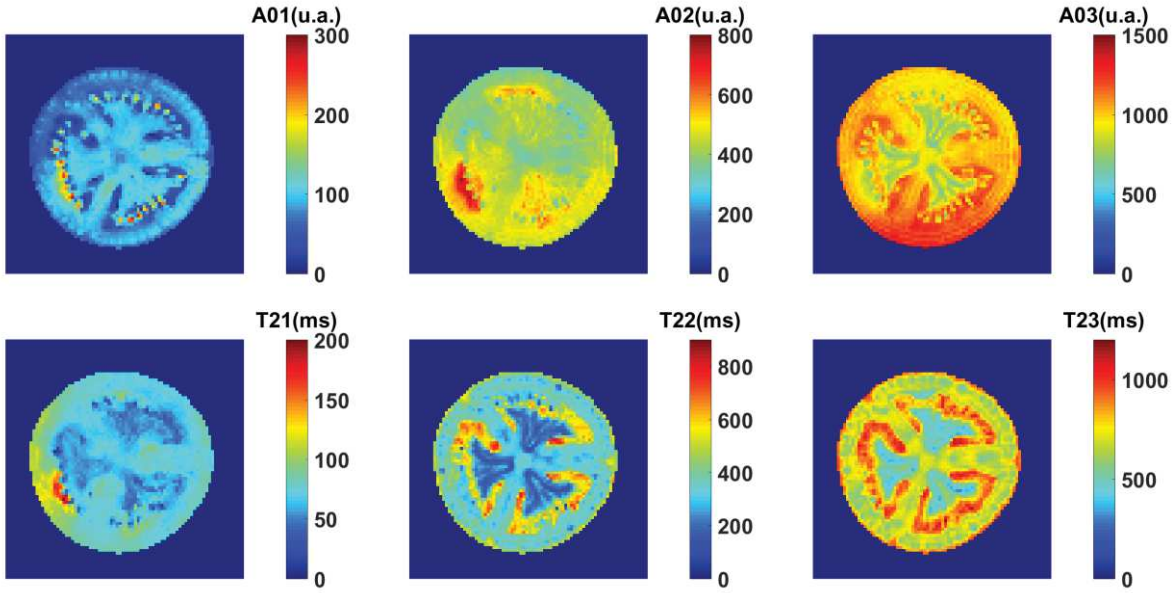

Figure 5

Click here to access/download;Figure;figure_5.docx

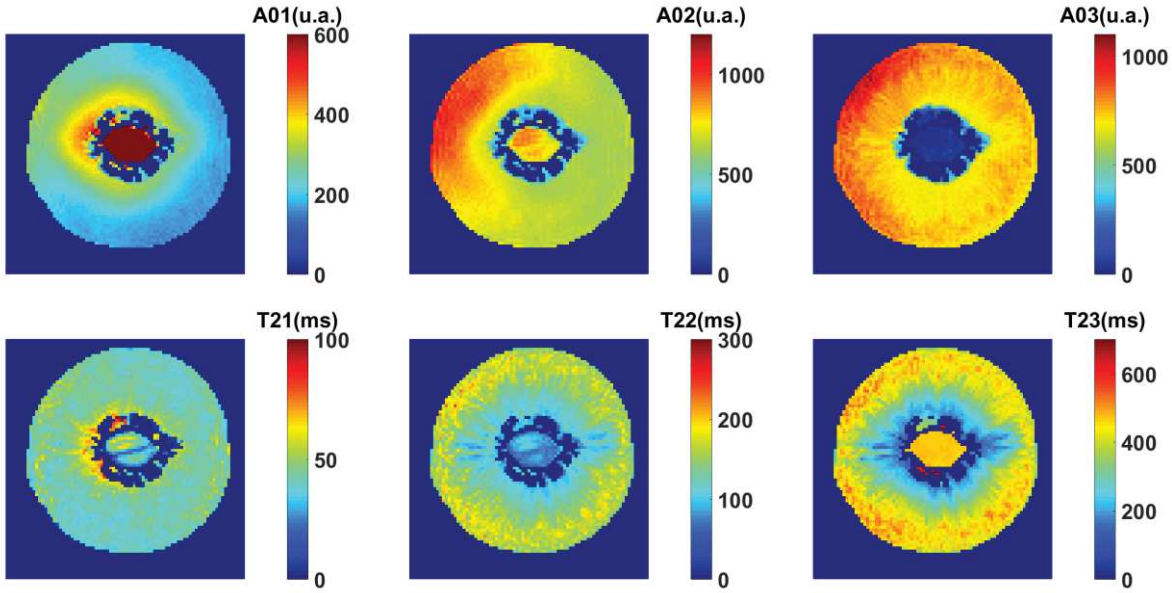

Figure 6

Click here to access/download;Figure;figure_6.docx

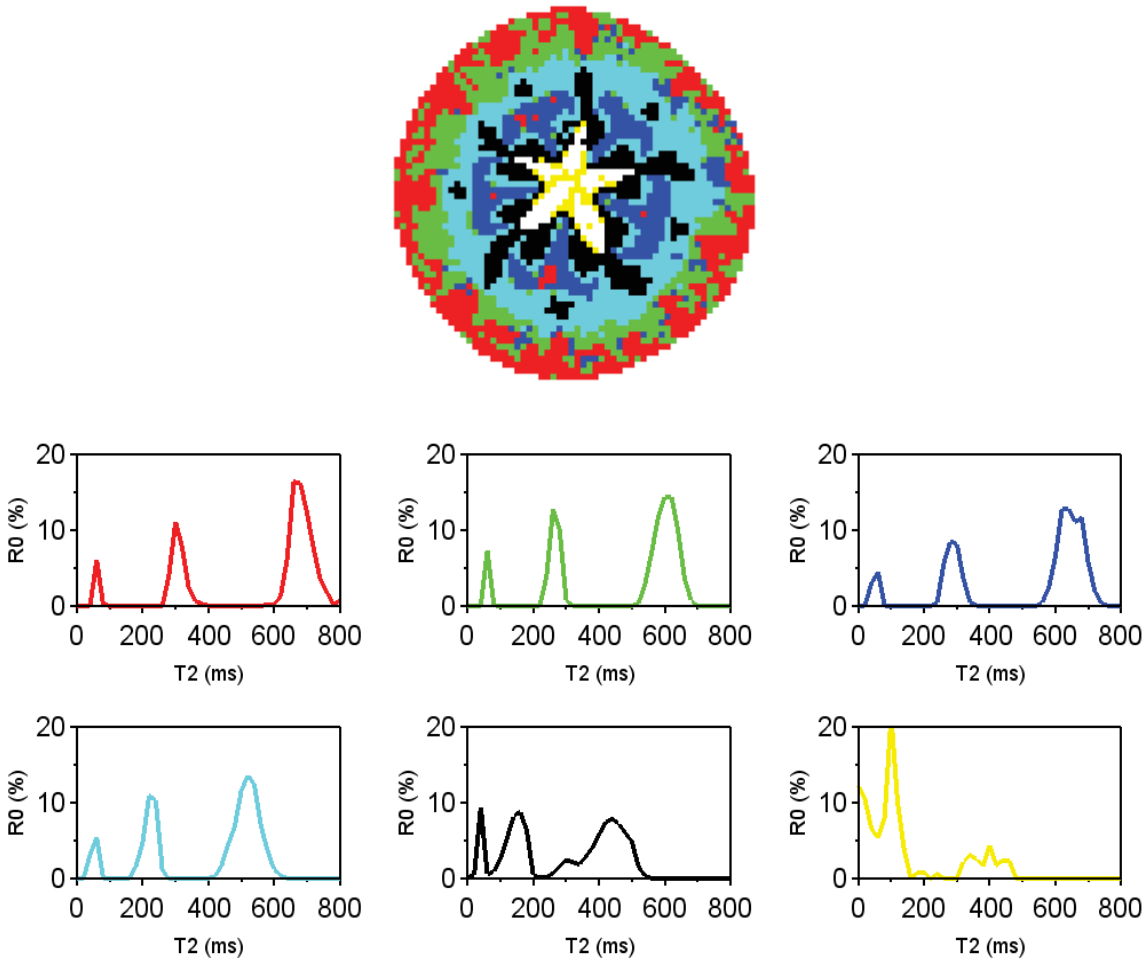

Figure 7

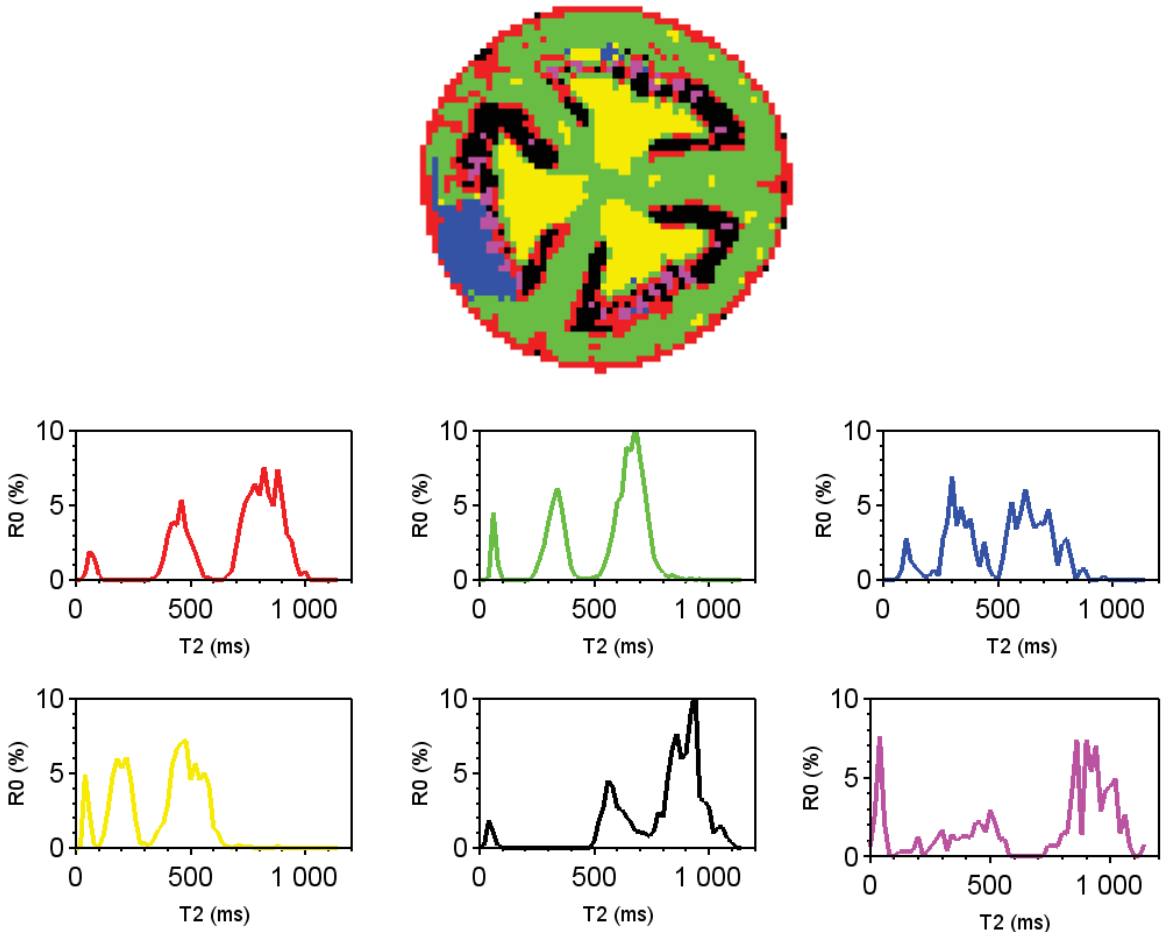

Figure 8

Click here to access/download;Figure;figure_8.docx

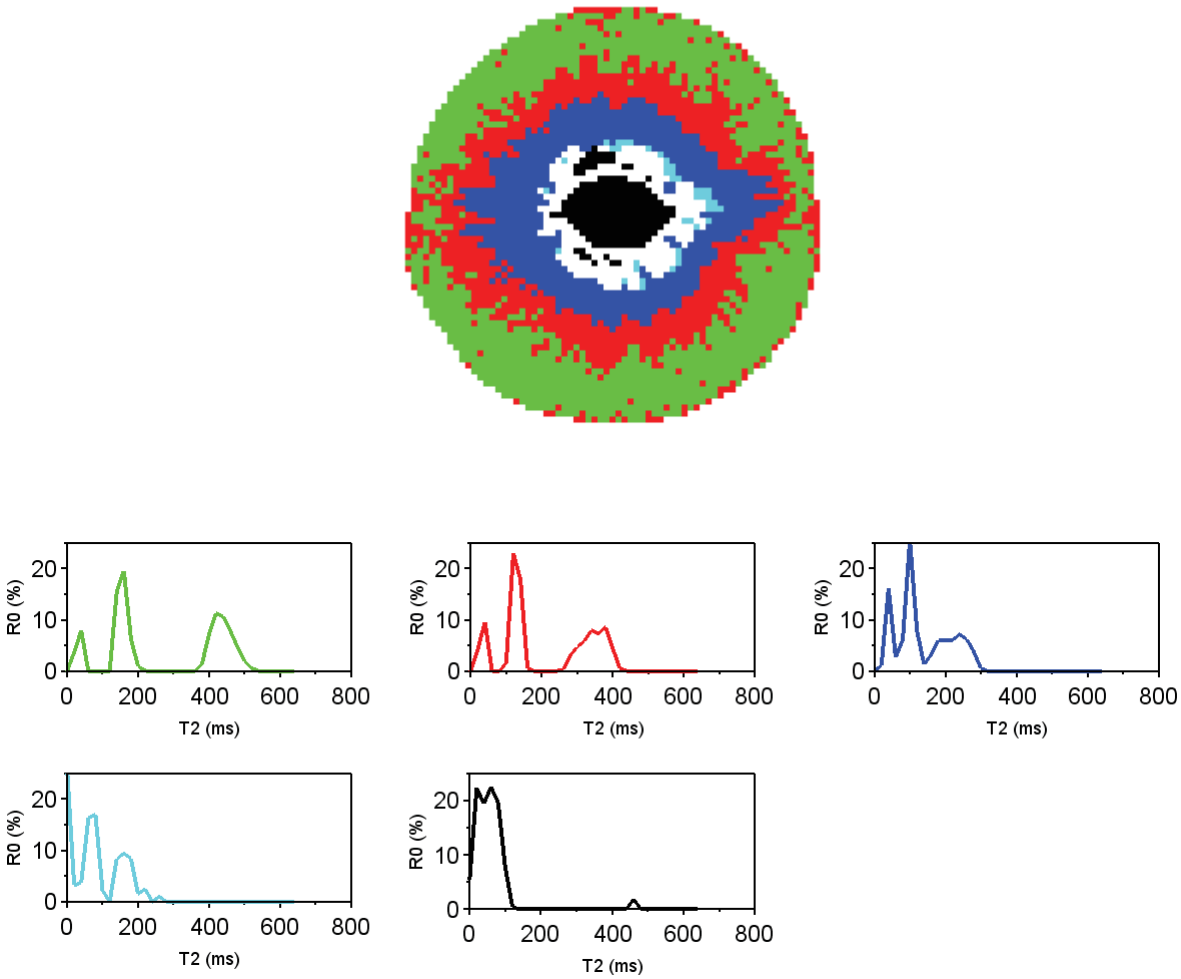

Figure 9

Click here to access/download;Figure;figure_9.docx

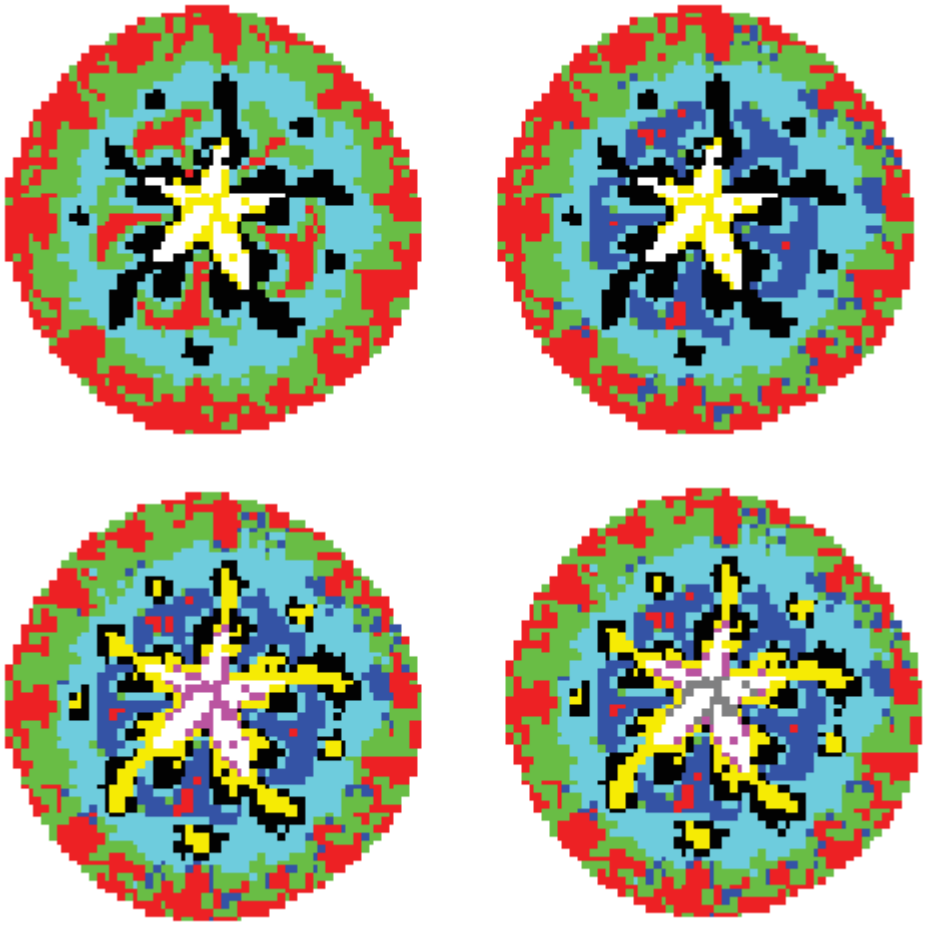

Figure A2.1 Click here to access/download;Figure;figure_A2.1.docx

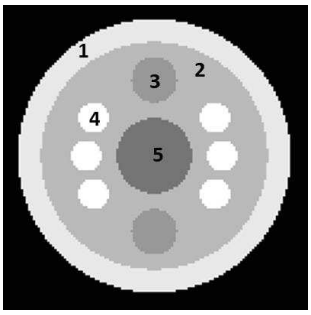

Figure A4.1

Click here to access/download;Figure;figure_A4.1.docx

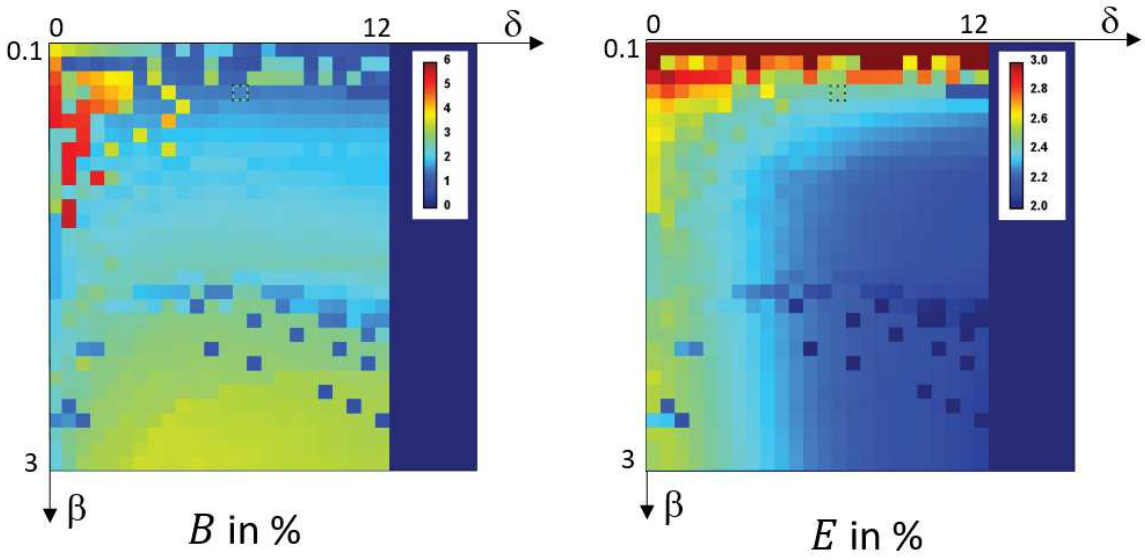

Author statement

The authors declare that the work described has not been published previously, that it is not under consideration for publication elsewhere, that its publication is approved by all authors and tacitly or explicitly by the responsible authorities where the work was carried out, and that, if accepted, it will not be published elsewhere in the same form, in English or in any other language, including electronically without the written consent of the copyright-holder.

Multi-exponential MRI T2 maps: a tool to classify and characterize fruit tissues

Authors : Guylaine Collewet, Maja Musse, Christian El Hajj, Saïd Moussaoui

1. Introduction

T_2 relaxation times and the associated signal amplitudes, obtained from a multi-spin echo signal, provide information on the microstructure and composition of samples. Since one voxel generally contains several types of tissue or different water pools with specific properties, the signal actually corresponds to a multi-exponential decay. In the case of brain imaging, multi-exponential T_2s are used for the quantification of myelin in the brain [1], where three major components can be identified: water trapped between the layers of the myelin sheath; intra/extracellular water; and cerebro-spinal fluid. In the case of fleshy fruit, water in different cell compartments limited by membranes has different chemical and physical properties, and therefore different T_2 times and self-diffusion coefficients.

Several mechanism govern relaxation. Additionally to molecular mobility, relaxation times depend on chemical exchange of water protons with macromolecules and solid surfaces. Consequently, relaxation times of water solutions in different cell compartments depend on their particular composition (solute type, concentration, pH) [2]. Relaxation times also depend on diffusional exchanges of water molecules between compartments separated by a membrane. These exchanges are modulated by their diffusion coefficients, cell membrane permeability and compartment size. In the case of slow and intermediate diffusional exchange, the resulting water relaxation signal is multi-exponential, reflecting water compartmentalization.

Assuming that a voxel in MRI image, or a sample in NMR experiment, represents a single tissue, T_2 decay signal components can be assigned to the water in the principal subcellular tissue compartments (vacuole, cytoplasm, cell wall) [3] or to the vacuoles of cell populations with distinct volume distributions [4, 5]. Several NMR studies successfully accessed information about water distribution and status and associated structural changes at cell and tissue levels in different fruits and vegetables undergoing physiological changes or subject to processing. For example, changes in structure and compositions in plant tissues were characterized during their development [6], ripening [7], drying [8] and thermal processes [9]. Such studies have also been performed by MRI, for example, in assessing fruit characteristics during development (in the case of apple and peach) [4], where changes in vacuole-

related transverse relaxation rates were mostly explained by cell/vacuole size. During apple storage, multi-relaxation times were correlated with the mechanical properties of the sample [10]. It is therefore possible to use MRI to access information on water status and distribution at the subcellular level on a whole fruit.

However, in the latter MRI studies [4, 10], multi-exponential T_2s were estimated at region of interest (ROI) level in order to increase the signal to noise ratio (SNR), to the detriment of spatial resolution. Indeed, the T_2 distribution for each water pool was estimated by the computation of an inverse Laplace transform, a procedure that is very sensitive to noise. Alternatively, a "discrete" model considering each component as a single T_2 with unknown value and amplitude has proven to be effective, at least for the estimation of the mean T_2 values of each distribution [11]. The number of components within each voxel can be considered to be known and of low value, bi or tri-exponential models are mostly used for biological tissues. However, this C-exponential model is still not straightforward to invert, in order to estimate the underlying relaxation time parameters, in the presence of noise.

A recently proposed method allows a joint estimation of relaxation time values T_2 and their amplitudes A_0 in each voxel to be carried out following a discrete model [12]. This work paves the way for the exploitation of multi-exponential information at voxel level in MRI. However, in the case of a C-exponential model, it is the total of $2C$ variables that is estimated in each voxel. The analysis of these results, consisting of multiple T_2 and A_0 maps, is consequently not straightforward and requires a post-processing scheme to be able to benefit from the information in an efficient way. Moreover, the intensity non-uniformity that is inherent in the MR images [13] is transferred automatically to the A_0 maps, a fact which may disrupt the analysis.

In this paper, we propose a post-processing scheme of the multiple T_2 and A_0 maps that clusters similar voxels in order to reduce the complexity of the information while avoiding the problems associated with intensity non-uniformity. Moreover, it is found that these clusters of voxels sharing the same T_2 distribution and A_0 values also corresponds to different tissues of the fruit. We also propose a data representation suitable for the visualization of the T_2 distribution within each cluster. We illustrate this approach with results for three different fruits, demonstrating the great potential of multi-T_2 information to shed new light on fruit characterization. A further important outcome of this work is the simplification it offers of the estimation method proposed in [12] by reducing the number of tuning parameters. Finally, we propose the use of a criterion designed for model order selection in order to determine the optimal number of components.

2. Material and methods

2.1 MRI image acquisitions

Images were acquired at ambient temperature on an apple, a tomato and a peach using a Multi-SE sequence [14] on a 1.5T MRI scanner (Magnetom, Avanto, Siemens, Erlangen, Germany) , with TE=6.5 ms, bandwidth of 260 Hz/pixel, 512 (tomato and apple) or 256 (peach) echoes per echo train and a repetition time of 10s. The median planes of the fruits were imaged with a slice thickness of 5 mm and a voxel size of 1.19 × 1.19 mm^2 for the tomato and apple, and 0.79 x 0.79 mm^2 for the peach. The number of averages was one for the apple and the tomato. For the peach with its smaller voxel size, the number of averages was four in order to compensate for the loss of signal and to recover a similar SNR. A head-array coil composed of 4 elements was used and its images were combined using a spatial matched filter [15]. In addition, data were acquired in a regular cartesian scheme and no post-processing was applied in order to obtain a non-stationary Rician noise.

2.2 Estimation of multi-exponential T_2 and A_0 maps

2.2.1 Estimation algorithm

In order to estimate the multi- T_2 and amplitude A_0 maps, we used the method described in [12]. It relies on a discrete model with an *a priori* known number of components. The method is based on the maximization of the likelihood of the data under the Rician noise hypothesis while imposing spatial regularity in the solutions in order to reduce the effects of the noise. The transverse relaxation signal in voxel x at time t without noise is modeled as:

$$s_{xt} = \sum_{c=1}^{C} A_{0cx} e^{-t/T_{2cx}} \qquad \text{(eq. 1)}$$

where A_{0cx} and T_{2cx} are respectively the amplitude and the relaxation time of component c in voxel x, and C is the number of components. This model is based on the hypothesis that indirect and stimulated echoes do not interfere with the acquired signal [16]. The proposed method can be summarized as the minimization of a criterion:

$$J = -\log(L) + R_{reg} \quad \text{(eq. 2)}$$

with

$$L = \prod_{x=1}^{X} \prod_{t=1}^{T} P_{\mathrm{Ric}}(y_{xt} | s_{xt}, \sigma_x^2) \quad \text{(eq. 3)}$$

and

$$R_{reg} = \sum_{p=1}^{P} \beta_p \sum_{x=1}^{X} \sum_{k \in V_x} \psi_p(\theta_{xp} - \theta_{kp}) \quad \text{(eq. 4)}$$

L is the likelihood of y_{xt}, the signal measured in voxel x at time t. σ_x is the standard noise deviation at voxel x and is assumed to be known. P_{Ric} is the Rician probability density function, T is the number of echoes, X the number of voxels. For R_{reg}, P is the number of parameters in each voxel equal to $2C$, θ_{xp} parameters p at voxel x (either A_{0cx} or T_{2cx}), V_x the set of neighboring voxels of x, and β_p a scalar that controls the weight of the regularization term for component p. In order to use the optimization scheme proposed in [12], the penalty function ψ_p must be a symmetric convex function. L2-L1 regularization, which corresponds to $\psi_p(u) = \sqrt{u^2 + \delta_p^2}$ is very interesting since it enables the preservation of the transitions between different tissues [17, 18]. However, tuning of the scalars β_p and δ_p might turn out to be impracticable since it comes down to the choice of a $2P$-uplet whose components might be interdependent. In order to overcome this issue, we propose, as suggested in [19], to define a new regularization term, R_{reg}^r, based on the relative difference of the parameters. This is written:

$$R_{reg}^r = \beta \sum_{p=1}^{P} \sum_{x=1}^{X} \sum_{k \in V_x} \psi(\theta_{xp} - \theta_{kp}) \quad \text{(eq. 5)}$$

with

$$\psi(\theta_{xp}, \theta_{kp}) = \frac{(\theta_{xp} - \theta_{kp})^2}{\theta_{xp} + \theta_{kp} + \delta|\theta_{xp} - \theta_{kp}|} \quad \text{(eq. 6)}$$

With this new definition of the regularization criterion, the number of tuning parameters reduces to two, β and δ, whatever the number of components C. As explained in Appendix 1, the use of the

chosen regularization function does not require the modification of the optimization algorithm proposed in [12] since the same minimization scheme proposed for J can be used in order to minimize $-\log(L) + R^r_{reg}$.

2.2.2 Initialization

The initialization of the estimation algorithm is an important step since non-adequate values could lead to estimation errors. Since we could draw on recorded measurements taken from regions of interest in fruits in previous experiments [20, 21], we initialized the algorithm with a priori known values for the relaxation times, T^i_{2c}, and relative amplitude values, R^i_{0c}. These values were the same for each voxel. The use of relative amplitude values for the initialization is relevant since they depend only on the observed object and not on parameters associated with the MR system such as receiver gain or the type of coil used, nor on spatial variations due to B_0 and B_1 non-uniformities. The initial amplitude values A^i_{0cx} at each voxel x were deduced using the following formula:

$$A^i_{0cx} = y_{xTE} \frac{R^i_{0c}}{\sum_{c=1}^{C} R^i_{0c} e^{-TE/T^i_{2c}}} \qquad \text{(eq. 7)}$$

Hence, this approach automatically takes the MRI acquisition process into account (ie the total gain of the reception scheme including its spatial non-uniformities which are part of y_{xTE}). For all subsequent analysis, we used the values of 80, 300 and 600 ms for the T^i_{2c} and for the corresponding R^i_{0c}, we used 0.06, 0.27 and 0.67.

In order to evaluate the sensitivity of the results regarding the initialization, we estimated A_0 and T_2 on the apple with different initial values, by testing all the combinations of $T^i_{2c} \pm aT^i_{2c}$ and $R^i_{0c} \pm aR^i_{0c}$ with a =0.1 and 0.2 (variations of 10% and 20% around the initial values). This corresponds to 2^{2C-1} different initialization given the constraint $\sum_{c=1}^{C} R^i_{0c} = 1$. We estimated for each voxel the standard variation of all the estimated values for each parameter.

2.2.3 Noise measurement

We place ourselves in the context of conventional MR image acquisition using a single-channel RF coil with a reconstruction using a Fourier transform and the computation of magnitude images. This results in a stationary noise, that is $\sigma_x = \sigma_0$ in each voxel, with Rayleigh statistics in background where no signal is present [22]. We neglected other unwanted fluctuations of the signal linked for example to

pulse errors, which may make the noise vary with the intensity of the signal, especially in the case of multi-echo acquisitions. . The estimator based on the first moment of the Rayleigh distribution gives:

$$\sigma_0 = \sqrt{\frac{2}{\pi}} \frac{1}{X_b} \frac{1}{T} \sum_{x \in \mathcal{B}} \sum_{t=1}^{T} y_{xt} \qquad \text{(eq. 8)}$$

where X_b is the number of voxels in the background. The measured SNR, defined as the mean value of the first echo divided by σ_0, was 116, 145 and 180 for apple, tomato and peach respectively.

2.2.4 Tuning the regularization parameters

The tuning of β and δ was realized using a virtual object described in Appendix 2. It is composed of five different virtual tissues, whose A_0 and T_2 values are in accordance with those observed in tomatoes in previous studies [14] for which a three exponential relaxation model was considered.

Images were simulated using similar parameters to those described in section 2.1 for the MR images. Stationary noise with a Rician distribution was incorporated into the simulated images. The SNR was set at 150.

The investigated value sets of the regularization parameters β and δ were, respectively, from 0.1 to 3 in steps of 0.1 and from 0.5 to 12 in steps of 0.5. We tested all value combinations. We initialized the algorithm with the actual values of the A_0 and T_2 parameters and, to provide indicators of the performance of the algorithm, we computed the bias B and standard deviation E of the relative estimation errors. B was defined as the mean of the absolute values of the biases over each region and parameter, in order to avoid any error compensation between regions or parameters (see Appendix 3).

We retained β and δ values for which B was low and in a relatively smooth region of the space (β, δ) in order to obtain a robust selection. Detailed results are presented in Appendix 4. The retained values were $\beta = 0.4$ and $\delta = 7$, which gave a total absolute bias B and a standard deviation E of 1.6% and 2.4%. Finally, the value of β was adjusted for each set of images in order to take the actual value of the noise σ_0 into account and ensure comparable weights between $-\log(L)$ and R_{reg}^r:

$$\beta \leftarrow \beta \frac{\sigma_0^2}{\sigma^2} \qquad \text{(eq. 9)}$$

This transformation was deduced from equation (24) in [12].

2.2.5 Choice of the number of components

The estimation algorithm relies on a *a priori* known number of components. In order to set it, we used the Bayesian Information Criterion (BIC) which is a criterion used for model order selection among a set of models [23]. It represents a compromise between the likelihood, the number of variables (model complexity). Indeed, the addition of parameters to the model (the increase of C in our case) might increase the likelihood but may also result in overfitting. To compensate this, the BIC criterion introduces a penalty term which takes into account the number of variables and the data size. It writes:

$$BIC = -2\log(L) + N_p \log(N_d), \quad \text{(eq.10)}$$

where N_p and N_d stands respectively for the number of variables and the number of data. The model order which gives the lowest BIC criterion is chosen.

The expression of the BIC in our case, averaged over all voxels, is:

$$\overline{BIC} = -\frac{2}{X}\log\left(\prod_{x=1}^{X}\prod_{t=1}^{T} P_{\mathrm{Ric}}(y_{xt}|s_{xt},\sigma^2)\right) + P\log(T) \quad \text{(eq.11)}$$

We computed the BIC criterion on each fruit for C=1 …5.

2.3 Classification of voxels

As explained previously, a post-processing scheme is proposed in order to enable the exploitation of the estimated maps which contain too much information for visual inspection to be able to offer optimal analysis and better characterization of the fruit tissues. We propose to collect similar voxels using a classical classification algorithm as explained below.

2.3.1 Classification

For the classification of the voxels, we focused on unsupervised algorithms. Indeed, the overall idea was to include as little *a priori* information as possible in order to determine what information was provided by the multi-exponential data. Among the available classification methods, we chose the K-Means clustering algorithm which aims to divide observations into a selected number of clusters where each observation belongs to the cluster with the nearest mean [24]. This method calls for the *a priori* specification of the number of classes. It was our view that the appropriate number of classes, or at least a good approximation of it, could be set by looking at the results for a range of class numbers

using a systematic trial and error approach. We accordingly increased the number of classes progressively until the visual results became too noisy to be interpreted.

Two normalization stages were applied beforehand. First, in order to get rid of spatial variations in the amplitudes linked to B_0 and B_1 non-uniformities, we adopted an approach similar to that in the initialization stage and relied on the relative values of each component rather than on their absolute amplitudes. Indeed, under the hypothesis that non-uniformity does not depend on the component and can be considered to be a multiplicative term, the signal with non-uniformities s_{xt}^{I} can be written as:

$$s_{xt}^{I}(\theta_x) = I_x \sum_{c=1}^{C} A_{0cx}^{*} e^{-t/T_{2cx}} \qquad \text{(eq. 12)}$$

where I_x stands for the non-uniformity factor in voxel x and A_{0cx}^{*} for the unbiased amplitude. The estimated amplitudes actually correspond to $A_{0cx} = I_x A_{0cx}^{*}$ and thus might be corrupted by spatial variations. In order to get rid of I_x we computed for each component and for each voxel the ratio R_{0cx} over the sum of the estimated amplitudes, which can be written as:

$$R_{0cx} = \frac{A_{0cx}}{\sum_{c=1}^{C} A_{0cx}} = \frac{I_x A_{0cx}^{*}}{\sum_{c=1}^{C} I_x A_{0cx}^{*}} = \frac{A_{0cx}^{*}}{\sum_{c=1}^{C} A_{0cx}^{*}} \qquad \text{(eq. 13)}$$

and gives rise to values that no longer depend on the multiplicative bias.

Second, in order to assign similar weightings to each variable in the classification process, the normalized parameter value θ_{xp}^{n} was computed using the following procedure:

$$\theta_{xp}^{n} = \frac{\theta_{xp}}{\max\left(\{\theta_{xp}\}_{x\in[1\ldots X]}\right)} \qquad \text{(eq. 14)}$$

The K-Means algorithm was applied to the set $\theta_{xp}^{n} = \{T_{2cx}^{n}, R_{0cx}^{n}\}$. The Matlab [25] implementation was used with default values and 60 replicates, that is, the number of times the clustering is repeated, each repetition having a new set of initial centroids.

2.3.2 Representation of class characteristics

In order to provide a representation of the T_2 values for each class, the distribution of the relaxation times was computed as follows: for each T_2 interval of width 20 ms, the corresponding R_0s were added for each component. The sum was divided by the number of voxels in each class in order to obtain comparable amplitude scales between classes. Thus, the distribution D was expressed as:

$$D(h) = \frac{1}{X}\sum_{c=1}^{C}\left(\sum_{x|H(h)<T2_{cx}\leq H(h+1)} R_{0cx}\right) \quad \text{(eq. 15)}$$

where H denotes the set of T_2 value intervals. This distribution is the sum of C distributions, each of the latter being obtained from the histogram of T_2 values of one component, weighted by the corresponding relative amplitudes.

2.3.3 Statistical tests

The differences between the classes were assessed statistically using a univariate approach. We focused on the difference between each pair of classes, which corresponds to the univariate post-hoc analysis of a multivariate analysis. The Shapiro-Wilk test was first used to determine if T_{2c} and R_{0c} values were normally distributed within each class. As they were not, the Kruskal-Wallis test was performed. The alpha level was set to 0.01 and the Bonferonni correction was used as the control for multiple comparisons between each pair of classes.

3. Results

3.1 Performance of the algorithm and choice of C

3.1.1 Estimation performance

We compared our results with those obtained using the method proposed in [12] where a L2 regularization function was used ($\psi_p(u) = u^2$), implying the tuning of $P = 2C$ parameters. We used the phantom images and initialized the results to the true value. The values of B_p and E_p are reported in Table 1 for all the parameters. We found very similar results showing that the new regularization scheme that we proposed, that is a L1-L2 regularization function based on the relative difference of

the parameters, did not lower the performance with the benefit to reduce the number of tuning parameters to two, whatever the number of components.

		A_{01}	T_{21}	A_{02}	T_{22}	A_{03}	T_{23}
B_p (in %)	L2 regularization [12].	2.67	4.15	1.49	1.36	0.85	0.3
	Current method	1.65	3.14	1.57	1.44	0.86	0.32
E_p (in %)	L2 regularization [12].	3.27	5.44	3.84	3.1	1.81	0.76
	Current method	3.62	5.15	1.99	2.23	0.9	0.5

Table 1: Bias and standard deviation of the relative estimation errors for the regularization scheme proposed in [12] and for the current method.

3.1.2 Choice of C

Figure 1 represents $\overline{BIC}$ for the three fruits for C=1 … 5 and, separately for each fruit, for C=2 … 5 for better visualization of the results in this range. These results clearly show the interest of multi-exponential estimation compared to mono exponential one since much lower BIC criterion were obtained for $C > 1$. For each of the three fruits, the lowest BIC value was observed for $C = 3$ and this number was consequently chosen for the analysis. However since this choice corresponded to a mean value over all the voxels, it was interesting to visualize the optimal number of components in each voxel. Figure 2 represents the number of components corresponding to the lowest BIC values for each voxel, for tomato, peach and apple from left to right. For peach, it can be observed that a three components model gave the lowest BIC for a majority of voxels, while a two components model would be the most appropriate in the zone around the stone, and four components would better suit some voxels in the pericarp area. For apple, for most of the voxels a two or a three components model would be the best, except for very few voxels for which four components would give the lowest BIC. Finally, for tomato, the results were similar as those observed on the apple, with a higher number of voxels corresponding to a four components model and some voxels even to a five components model.

3.1.3 Robustness of the initialization

Variation of the initialization on the apple was realized using $C = 3$ which led to 32 different initialization sets. Table 2 shows the mean standard deviation (computed over all the voxels) expressed in percentage of the mean estimated value for each parameters and for a variation of 10% and 20% of the initialization.

Variation of the initial values	A_{01}	T_{21}	A_{02}	T_{22}	A_{03}	T_{23}
10%	5.79	5.22	5.27	4.05	2.8	1.02
20%	10.7	8.95	9.37	7.74	5.49	1.88

Table 2: Relative mean standard deviation (in %) for each parameters for the 32 different initialization sets of values in the case of apple.

As expected, the parameters corresponding to the longest T_2 are less sensitive to the initial values, especially T_{23} for which the standard deviation is smaller than 2% of the mean value. With a variation of 20% of the initial values, the standard deviation goes up to 10.7% for A_{01} what remains acceptable. These results highlight the importance of the initialization, while showing that by remaining within a reasonable range of variation for the initialization, the results vary in a relatively small way.

3.2 T_2 and A_0 maps on fruit

The estimated T_2 and A_0 maps for apple, tomato and peach are shown in Figures 3, 4 and 5 respectively. For all these fruits, the different structures could be clearly observed, particularly on the T_{22} and T_{23} maps which displayed the greatest contrasts between the tissues. In the apple, the core and vascular bundles could be distinguished from the other tissues on both the T_2 and A_0 maps, while in the mesocarp tissue, the T_{22} and T_{23} values progressively increased from the inner region to the region near the cuticle. The endocarp corresponded to the star-shaped hole in the fruit center. In the tomato, the locular tissue containing the seeds and the placenta were distinguishable from the equatorial and radial pericarps. Last, in the peach, it was possible to see the seed but not the endocarp, the latter appearing as a lack of MRI signal in the middle of the fruit, while the values for T_{22} and T_{23} showed a smooth gradation without strong contrasts from the seed to the cuticle.

3.3 Classification and T2 distribution

3.3.1 Results for apple

Figure 6 represents the classification results on apple using six classes and the corresponding T_2 distributions. The p-values for each variable and each pair of classes are given in Table 3.

		T_{21}	R_{01}	T_{22}	R_{02}	T_{23}	R_{03}
R	G	2.46E-03	2.11E-63	2.58E-76	1.16E-39	7.43E-78	7.24E-66
R	B	8.72E-137	1.28E-56	1.54E-13	4.97E-04	8.16E-13	1.08E-24
R	C	8.97E-161	1.27E-282	6.34E-273	9.45E-165	1.52E-275	2.51E-253
R	Bk	4.59E-278	0.00E+00	0.00E+00	6.07E-277	0.00E+00	0.00E+00
R	Y	2.98E-75	1.17E-91	5.31E-85	8.60E-72	2.93E-79	2.37E-86
G	B	7.31E-101	1.00E+00	5.85E-18	8.29E-14	1.72E-19	9.06E-06
G	C	8.75E-116	1.40E-73	2.95E-56	2.36E-40	4.39E-56	8.30E-57
G	Bk	2.83E-226	5.27E-148	4.07E-124	2.07E-124	1.75E-115	1.50E-130
G	Y	1.22E-63	5.80E-42	6.65E-34	2.25E-36	5.99E-30	1.14E-37
B	C	1.00E+00	1.45E-53	1.49E-120	1.24E-88	2.36E-124	2.33E-83
B	Bk	6.68E-25	8.14E-119	2.00E-195	6.31E-183	1.01E-189	6.92E-159
B	Y	1.31E-12	1.42E-38	2.25E-56	4.53E-56	2.00E-52	2.16E-49
C	Bk	4.88E-38	3.84E-26	5.86E-25	5.27E-36	3.46E-21	1.28E-27
C	Y	2.61E-15	1.57E-10	5.32E-09	2.47E-13	4.97E-07	6.56E-11
Bk	Y	2.91E-01	8.17E-01	1.00E+00	7.75E-01	1.00E+00	8.39E-01

Table 3: p-values for each pair of classes and each variable in apple. Values > 0.01 are shown in grey. Single initials are used to designate colors of classes except black (Bk).

Although no spatial information was introduced for the classification step, the region obtained appears spatially consistent in the classification map. It is to be noted that the use of amplitude proportions

rather than absolute values made it possible to group voxels together in a single class despite their differing absolute values, the latter being the consequence of MR non-uniformities that can clearly be seen in the second and third amplitude images in Figure 3.

Looking at distribution, it appears that each component contributed to only one peak, which means that the ranges of low, medium and high T_2 did not overlap across the set of voxels. Thus, in each curve, the three different components could clearly be distinguished, except for that shown in yellow which corresponds to only a few voxels situated in (or between) the seeds.

The apple mesocarp was divided into three different classes, of which two (red and green) were imbricated one in the other, while the third (cyan) bordered the core. These classes differed in T_{22} and T_{23}, where progressive increases occurred in mean values from ~233 to 318 ms (T_{22}), and from 529 to 695 ms (T_{23}), from cyan to red through green. The class shown in blue corresponded to the core. In the black zone, both petal and sepal bundles could be distinguished.

Statistical analysis showed that there was no statistical difference between the black and yellow classes which could be considered as one class (p-values >0.01). For the four other classes, only two variables showed no statistical differences, R_{01} between green and blue and T_{21} between blue and cyan. For the other cases, the p-values exhibit a statistical difference between these classes. This is particularly interesting for the red, green and cyan classes. They correspond to the same tissue in the apple (the mesocarp) and reveal that it is not homogeneous.

3.3.2 Results for tomato

Figure 7 represents the classification results for tomato using six classes and the corresponding T_2 distributions. The p-values for each variable and each pair of classes are given in Table 4.

		T_{21}	R_{01}	T_{22}	R_{02}	T_{23}	R_{03}
R	G	3.73E-03	9.71E-81	4.29E-115	6.89E-10	1.36E-116	6.39E-42
R	B	4.17E-33	5.55E-38	9.77E-36	3.52E-99	9.61E-42	8.88E-112
R	Y	3.36E-124	4.78E-211	3.84E-305	1.64E-153	6.46E-296	1.52E-221
R	Bk	2.64E-81	1.28E-03	3.11E-17	6.28E-04	2.47E-07	1.54E-09
R	M	1.16E-52	8.26E-103	3.09E-05	1.00E+00	3.78E-04	1.42E-49
G	B	8.62E-52	2.47E-01	1.00E+00	9.46E-78	1.00E+00	1.63E-55
G	Y	7.15E-131	3.99E-71	5.31E-104	2.63E-134	2.13E-96	2.13E-127
G	Bk	8.72E-78	5.93E-98	2.55E-195	3.76E-24	2.33E-153	3.95E-82
G	M	6.11E-46	5.48E-42	4.03E-07	1.00E+00	1.83E-49	2.07E-19
B	Y	9.39E-175	3.99E-15	8.69E-37	3.70E-02	3.09E-29	1.00E+00
B	Bk	1.22E-139	2.82E-51	1.64E-73	2.86E-117	3.68E-64	1.10E-148
B	M	2.15E-102	3.77E-22	1.39E-04	1.33E-38	6.73E-37	3.90E-01
Y	Bk	1.17E-01	2.95E-223	0.00E+00	3.24E-171	0.00E+00	1.06E-269
Y	M	9.99E-02	7.73E-06	1.46E-50	3.53E-36	2.36E-123	6.57E-01
Bk	M	4.55E-04	5.75E-118	2.53E-20	5.60E-03	1.00E+00	1.55E-72

Table 4: p-values for each pair of classes and each variable in tomato. Values > 0.01 are shown in grey. Single initials are used to designate colors of classes except black (Bk).

The different tissues could be distinguished on the classification map. The placenta appears in yellow, the locular tissue in black and the seeds in magenta. The voxels in red are in the peripheral area lying just under the cuticle. The core, the radial and the equatorial pericarp have been placed in the same class, shown in green. The class shown in blue corresponds to a particular zone that covers both the locular tissue and pericarp and which probably indicates an internal defect in the fruit.

Statistical analysis showed that for each pair of classes, at least one variable was statistically different. However, some similarities were found between the green and blue classes, for which , only the lowest one among T_2 values was different.

It can be observed in the distribution that the highest T_{22} and T_{23} values were found in the locular tissue and the lowest in the placenta which is in accordance with observations in [26]. The distribution in the seeds suggests a two-component behavior, however this should not be over-interpreted since the number of voxels in this class is rather low. Further, given the small seed size and the spatial resolution of the MRI images, the partial volume effect is likely to have biased the results. The difference between the blue and green zones, which could be expected to be gathered regarding their spatial arrangement, was the effect, not of T_{22}, T_{23} or R_{01}, but of the amplitudes and the higher blue-zone values in T_{21}.

3.3.3 Results for peach

Figure 8 represents the classification results for peach using five classes and the corresponding T_2 distributions. The p-values for each variable and each pair of classes are given in Table 5.

		T_{21}	R_{01}	T_{22}	R_{02}	T_{23}	R_{03}
R	G	1.00E+00	1.81E-123	5.00E-192	2.25E-03	2.44E-210	5.13E-89
R	B	7.37E-97	5.12E-94	1.99E-71	2.74E-153	1.98E-77	1.04E-40
R	C	1.86E-19	1.98E-17	3.51E-17	8.11E-11	1.06E-12	4.36E-17
R	Bk	4.82E-03	1.65E-84	1.35E-60	2.14E-55	6.70E-85	1.19E-83
G	B	3.54E-103	0.00E+00	0.00E+00	3.99E-139	0.00E+00	7.50E-237
G	C	7.05E-21	1.11E-49	9.84E-60	3.12E-08	2.11E-53	3.33E-43
G	Bk	3.11E-04	5.70E-235	2.12E-235	2.82E-73	2.71E-03	6.38E-207
B	C	1.08E-53	1.52E-01	1.49E-02	1.00E+00	8.96E-01	6.56E-05
B	Bk	2.28E-56	2.10E-10	8.86E-07	2.86E-213	3.00E-201	1.42E-26
C	Bk	3.02E-11	1.00E+00	1.00E+00	3.86E-41	5.33E-56	1.00E+00

Table 5: p-values for each pair of classes and each variable in peach. Values > 0.01 are shown in grey. Single initials are used to designate colors of classes except black (Bk).

The spatial distribution of the classes was concentric with a decrease in T_{22} and T_{23} values from the periphery to the center, as can be seen in the T_2 distributions. Moreover, it can be observed that the distance between the peaks decreased from the periphery to the center suggesting that the differentiation between the characteristics of the water pools was more marked in the peripheral regions of the mesocarp. The black class represents the seed for which, obviously, the one component model seemed a better fit.

Statistical analysis showed that the green, red and blue classes could be considered to differ and this, as for apple, indicates a heterogeneity in the mesocarp tissue. The blue and cyan classes could be considered to be similar which is consistent with their location.

4. Discussion

Using the method described in [12] we were able to estimate the multi-T_2 relaxation parameters in each voxel. Thanks to the spatial regularization scheme, the ill-posed inverse problem could be solved despite the presence of noise. We provided a simplification of this method by reducing the number of scalar parameters needing to be tuned. However, we can propose a number of possible improvements to this method that can be explored further.

The initialization scheme is a well-known problem that could not be fully automated and required a degree of prior knowledge to set the parameters. Varying the initialization up to 20% led to acceptable variation in the estimated results in the case of apple. However, this point remains an important question and to this day not fully resolved. Nevertheless, by choosing to use amplitude proportions rather than absolute values in the initialization, we have provided a solution which is dependent neither on the receive coil nor the position of the fruit in the MR system. Further, the initialization step could be improved by using measurements taken from a large ROI to produce the initial estimate, giving a higher SNR.

The signal model used in this study assumes that indirect and stimulated echoes do not interfere with the acquired signal. However, the MSE sequence employs 180° refocusing pulses, which are imperfect and are sensitive to static and Radio Frequency and magnetic field imperfections, leading to corruption of relaxation curves by unwanted signals and to the introduction of T1 dependence on the T2 relaxation decay [27]. The application of constant crusher gradients and the use of non-selective rectangular refocusing pulses only partially correct for this effect. The extended phase graph (EPG) algorithm for simulating and correcting undesired signal [28] can be considered in future investigations.

The proposed method requires knowledge of the number of components, which must be the same for all voxels. The use of the statistical BIC criterion converged to the same number of components as in choice that we would have made a priori given our previous knowledge on the subject. However, the analysis of this criterion at the voxel level revealed that the optimal solution would be to consider a variable number of components in the image. However, since the spatial regularization assumes similar number of components in all voxels, we noticed that over estimating the number of components in some voxels will be compensated by the estimation of small amplitude values of the added component.

In the classification stage, the use of the relative amplitudes was very efficient in eliminating the effects of the spatial variation in intensity that was the result of the non-homogeneities of the MR system.

This, coupled with the use of relative amplitudes for initialization, gives our approach robustness regarding MR configuration and fruit position.

With regard to the choice of the number of classes, it appears that this was not a critical issue since it was possible to observe results involving different numbers of classes so as to select the optimal number of classes for spatial consistency. Moreover, the use of statistical analysis provided supplementary information on the actual differences between the classes. Figure 9 shows results for different numbers of classes for apple, from 5 to 8. The solution with 6 classes appeared optimal since it represented a compromise between the number of zones providing the greatest spatial consistency and that required to avoid an overly noisy result.

Previous studies have shown MRI relaxometry to be effective in discriminating between different fruit tissues [26, 29, 30] and in accessing their heterogeneity [4, 21, 31] in relation to spatial variations in biophysical and metabolic traits. However, thus far, multi-exponential relaxation times for tissues and/or tissues regions have been compared using an approach in which ROIs were selected manually from homogeneous regions of mono-exponential T2 maps and were considered to have homogeneous multi-exponential T2. The main limitation of this approach is that the latter condition is not always met. The post-processing classification scheme proposed in the present study overcomes this constraint. It has made it possible to confirm the heterogeneity of the apple and peach mesocarps observed in [4], providing improved accuracy in the delimitation of regions with similar relaxation parameters. It offers a promising tool to reveal greater detail in the spatial variations of multi-exponential relaxation parameters and, thereby, in water status and distribution at the subcellular level. This would probably assist in the elucidation of the nature of the relaxation mechanism that produces different multi-exponential transverse relaxation times throughout the mesocarp regions, which is still an open question. Last, this detection and classification method would be of benefit to the detection via MR relaxometry of the microstructural changes in fruit or tuber tissues that cause imperfections using the localized modifications in relaxation parameters

5. Conclusion

Fleshy fruits are generally considered as an assemblage of homogeneous tissues, due to the complexity involved in accessing experimental data on spatial variations in tissue characteristics using current analytical methods. However, the heterogeneity of fruit tissues is an important factor in physiological

processes as well as in fruit processing capability and quality. MRI relaxometry has great potential in providing a spatial analysis of tissue microstructure, making it possible to access information at the cellular and subcellular scales via multi-exponential relaxation times.

Despite this potential, the estimation of the relaxation parameters is an ill-posed problem and the exploitation of the results, which take the form of a number of parameter maps, may be not straightforward. We therefore first proposed a simplification of the method set out in [12] to estimate T_2s and their associated amplitudes, by reducing the number of spatial regularization parameters needing to be tuned. The number of component was chosen using a statistical criterion. A classification scheme based on K-Means was used to group voxels exhibiting similar values. MR non-uniformities did not affect the results thanks to the use of relative amplitudes. The classes were spatially consistent, demonstrating the relevance of our approach. Statistical analysis showed that most of the chosen classes were different. In order to visualize the characteristics of each class we proposed the representation of T_2 value distributions, which paves the way for further interpretation concerning tissue properties.

The initialization of the estimation algorithm is a matter that still remains to be solved. Inappropriate initialization has the potential to generate biased estimations. The approach we propose assumes that the number of components is the same in each voxel which may not be the case. For the classification step, it would be possible to introduce classification methods such as Markov fields or Gaussian mixture models with automatic estimation of the number of classes. Compared to the K-Means method, Gaussian mixture clustering would have the additional advantage of taking the variance of the measurements into account and would also calculate a probability for each voxel's membership of each class. On the other hand, the use of Markov fields would add the spatial information required to achieve clustering, offering a definitive way to eliminate the possible impact of noise on the clustering.

Appendix

Appendix 1

The minimization of J (eq. 1) is not straightforward. Indeed, the terms are not quadratic, $-\log(L)$ because of the expression of the Rician probability function, and R_{reg} because of the properties of functions ψ_p. Morever the problem is non-separable since R_{reg} depends on all the voxels simultaneously. In [12] a method is proposed that is carried out iteratively. At each iteration, $-\log(L)$

is majorized by a quadratic function and R_{reg} by a function which makes the problem separable. An adapted Levenberg-Marquardt algorithm is used at each iteration to impose a sufficient decrease of the objective function and the non-negativity of the parameters.

Interestingly, it has been shown in [19] that a majorant function of R_{reg}^{r} at iteration m can also be established. It is written as:

$$M_{REG} = \beta \sum_{p=1}^{P} \sum_{x=1}^{X} \sum_{k \in V_x} \frac{\left(2\theta_{xp} - \left(\theta_{xp}^{m} + \theta_{kp}^{m}\right)\right)^2}{2\theta_{xp} + \left(\theta_{xp}^{m} + \theta_{kp}^{m}\right) + \delta\left|2\theta_{xp} - \left(\theta_{xp}^{m} + \theta_{kp}^{m}\right)\right|}$$

The same approach as in [12] can thus be used for this regularisation term.

Appendix 2

The parameters of the estimation algorithm were tuned using a virtual object shown in Figure A2-1. It is composed of five different virtual tissues, the amplitudes and T_2 values of which are given in Table A2.1. These values are in accordance with those observed in tomatoes in previous studies [14] for which a three-exponential relaxation model was used.

Region	A_{01}(a.u)	T_{21}(ms)	A_{02}(a.u)	T_{22}(ms)	A_{03}(a.u)	T_{23}(ms)
1	95	88	459	356	1015	716
2	96	76	410	433	1024	870
3	109	78	375	303	1004	685
4	108	50	482	202	756	508
5	71	50	339	218	908	627

Table A2-1 : Amplitudes and T_2 values for the different tissues

Appendix 3

The tuning of the algorithm parameters was carried out using absolute bias B and standard deviation E defined as follows, where R is the number of tissues, X_r the number of voxels for tissue r, θ_{xp}^{*} and θ_{xp} the actual and estimated values of parameter p in voxel x:

$$B = \overline{B_p} \text{ with } \quad B_p = \frac{1}{R}\sum_{r=1}^{R}\left|\frac{1}{X_r}\sum_{x\in r}\frac{\theta_{xp}-\theta^*_{xp}}{\theta^*_{xp}}\right| \qquad \text{(eq.A3.1)}$$

and $E = \overline{E_p}$ with

$$E_p = \frac{1}{R}\sum_{r=1}^{R}\sqrt{\frac{1}{X_r-1}\sum_{x\in r}\left(\frac{\theta_{xp}-\theta^*_{xp}}{\theta^*_{xp}}-\frac{1}{X_r}\sum_{x\in r}\frac{\theta_{xp}-\theta^*_{xp}}{\theta^*_{xp}}\right)^2} \qquad \text{(eq.A3.2)}$$

Appendix 4

Figure A4.1 shows B and E as functions of β and δ, expressed in percentages. We retained β and δ values for which B was low and in a relatively smooth region of the space (β, δ) in order to obtain a robust selection. The retained values, outlined by dotted lines, were $\beta = 0.4$ and $\delta = 7$.

T

Acknowledgements

We are most grateful to the PRISM core facility (Rennes-Angers, France) for access to its facilities, and to GIS Biogenouest.

References

1. Laule, C., et al., *Magnetic resonance imaging of myelin.* Neurotherapeutics, 2007. **4**(3): p. 460-484.
2. Leforestier, R., F. Mariette, and M. Musse, *Impact of chemical exchange on transverse relaxation at low and moderate magnetic field strengths for sugar solutions representative of fruit tissues analyzed by simulation and MRI experiments.* Journal of Magnetic Resonance, 2021. **322**.
3. Van As, H., *Intact plant MRI for the study of cell water relations, membrane permeability, cell-to-cell and long distance water transport.* Journal of Experimental Botany, 2007. **58**(4): p. 743-756.

4. Musse, M., et al., *Spatial and temporal evolution of quantitative magnetic resonance imaging parameters of peach and apple fruit - relationship with biophysical and metabolic traits.* Plant Journal, 2021. **105**(1): p. 62-78.
5. Leforestier, R., F. Mariette, and M. Musse, *MRI Study of Temperature Dependence of Multi-exponential Transverse Relaxation Times in Tomato.* Applied Magnetic Resonance, 2021. **Early access**.
6. Sorin, C., et al., *Assessment of nutrient remobilization through structural changes of palisade and spongy parenchyma in oilseed rape leaves during senescence.* Planta, 2015. **241**(2): p. 333-346.
7. Raffo, A., et al., *Ripening of banana fruit monitored by water relaxation and diffusion H-1-NMR measurements.* Food Chemistry, 2005. **89**(1): p. 149-158.
8. Hills, B.P. and B. Remigereau, *NMR studies of changes in subcellular water compartmentation in parenchyma apple tissue during drying and freezing.* International Journal of Food Science and Technology, 1997. **32**(1): p. 51-61.
9. Gonzalez, M.E., et al., *1H-NMR Study of the Impact of High Pressure and Thermal Processing on Cell Membrane Integrity of Onions.* Journal of Food Science, 2010. **75**(7): p. E417-E425.
10. Winisdorffer, G., et al., *Analysis of the dynamic mechanical properties of apple tissue and relationships with the intracellular water status, gas distribution, histological properties and chemical composition.* Postharvest Biology and Technology, 2015. **104**: p. 1-16.
11. Andrews, T., et al., *Testing the three-pool white matter model adapted for use with T-2 relaxometry.* Magnetic Resonance in Medicine, 2005. **54**(2): p. 449-454.
12. El Hajj, C., et al., *Multi-exponential Transverse Relaxation Times Estimation from Magnetic Resonance Images under Rician Noise and Spatial Regularization.* IEEE Transactions on Image Processing, 2020. **29**: p. 6721-6733.
13. Ganzetti, M., N. Wenderoth, and D. Mantini, *Intensity Inhomogeneity Correction of Structural MR Images: A Data-Driven Approach to Define Input Algorithm Parameters.* Frontiers in Neuroinformatics, 2016. **10**.
14. Adriaensen, H., et al., *MSE-MRI sequence optimisation for measurement of bi- and tri-exponential T2 relaxation in a phantom and fruit.* Magnetic Resonance Imaging, 2013. **31**(10): p. 1677-1689.
15. Walsh, D.O., A.F. Gmitro, and M.W. Marcellin, *Adaptive reconstruction of phased array MR imagery.* Magnetic Resonance in Medicine, 2000. **43**(5): p. 682-690.
16. McPhee, K.C. and A.H. Wilman, *Transverse relaxation and flip angle mapping: Evaluation of simultaneous and independent methods using multiple spin echoes.* 2017. **77**(5): p. 2057-2065.
17. Charbonnier, P., et al., *Deterministic edge-preserving regularization in computed imaging.* IEEE Transactions on Image Processing, 1997. **6**(2): p. 298-311.
18. Idier, J., *Convex half-quadratic criteria and interacting auxiliary variables for image restoration.* IEEE Transactions on Image Processing, 2001. **10**(7): p. 1001-1009.
19. Nuyts, J., et al., *A concave prior penalizing relative differences for maximum-a-posteriori reconstruction in emission tomography.* IEEETransactions on Nuclear Science, 2002. **49**(1): p. 56-60.
20. Musse, M., et al., *Monitoring the postharvest ripening of tomato fruit using quantitative MRI and NMR relaxometry.* Postharvest Biology and Technology, 2009. **53**(1-2): p. 22-35.
21. Winisdorffer, G., et al., *MRI investigation of subcellular water compartmentalization and gas distribution in apples.* Magnetic Resonance Imaging, 2015. **33**(5): p. 671-680.
22. Aja-Fernández, S. and G. Vegas Sánchez-Ferrero, *Statistical Analysis of Noise in MRI*. 2016.
23. Schwarz, G., *Estimating the dimension of a model.* Annal of Statistics, 1978. **6**: p. 461-464.
24. MacQueen, J.B. *Some methods for classification and analysis of multivariate observations*. in *Fifth Berkeley symposium on mathematical statistics and probability* 1967. Berkeley, California, USA: University of California Press.
25. MATLAB, *version 9.1.0.441655 (R2016b)*. 2016: The MathWorks Inc.

26. Musse, M., et al., *An investigation of the structural aspects of the tomato fruit by means of quantitative nuclear magnetic resonance imaging.* Magnetic Resonance Imaging, 2009. **27**(5): p. 709-719.
27. Poon, C.S. and R.M. Henkelman, *Practical T2 quantitation for clinical applications.* Journal of Magnetic Resonance Imaging, 1992. **2**(5): p. 541-553.
28. Weigel, M., *Extended Phase Graphs: Dephasing, RF Pulses, and Echoes - Pure and Simple.* Journal of Magnetic Resonance Imaging, 2015. **41**(2): p. 266-295.
29. Ciampa, A., et al., *Seasonal chemical-physical changes of PGI Pachino cherry tomatoes detected by magnetic resonance imaging (MRI).* Food Chemistry, 2010. **122**(4): p. 1253-1260.
30. Clark, C.J. and J.S. MacFall, *Quantitative magnetic resonance imaging of 'Fuyu' persimmon fruit during development and ripening.* Magnetic Resonance Imaging, 2003. **21**(6): p. 679-685.
31. Defraeye, T., et al., *Application of MRI for tissue characterisation of 'Braeburn' apple.* Postharvest Biology and Technology, 2013. **75**: p. 96-105.

CAPTIONS

Figure 1: Mean BIC in function of the number of components C used in the model, on top left for the three fruits (C=1…5), the other subplots are for one fruit each (C=2…5)

Figure 2: Maps of the optimal values of number of components for the tomato, peach and apple, from left to right

Figure 3: Results for an apple. Amplitudes are shown on the top row and T_2s on the bottom row, with the shortest T_2 shown in the left column and the longest in the right.

Figure 4: Results for a tomato. Amplitudes are shown on the top row and T_2s on the bottom row, with the shortest T_2 shown in the left column and the longest in the right.

Figure 5: Results for a peach. Amplitudes are shown on the top row and T_2s on the bottom row, with the shortest T_2 shown in the left column and the longest in the right.

Figure 6: Classification map and relative amplitudes as a function of T_2 values for each class in apple.

Figure 7: Classification map and relative amplitudes as a function of T_2 values for each class in tomato.

Figure 8: Classification map and relative amplitudes as a function of T_2 values for each class in peach.

Figure 9: Classification results for apple with 5, 6 ,7 and 8 classes from left to right and top to bottom.

Figure A2.1: virtual phantom

Figure A4.1 B and E as functions of β and δ, computed on phantom simulations where the initialization is equal to the actual value. The square with a dotted outline indicates the chosen values.